CHEMISTRY OF MATERIALS

Article

pubs.acs.org/cm

Rechargeable Zinc Alkaline Anodes for Long-Cycle Energy Storage

Damon E. Turney,*[,†] Joshua W. Gallaway,[†] Gautam G. Yadav,[†] Rodolfo Ramirez,[†] Michael Nyce,[†] Sanjoy Banerjee,[†] Yu-chen Karen Chen-Wiegart,[‡] Jun Wang,[‡] Michael J. D'Ambrose,[†] Snehal Kolhekar,[†] Jinchao Huang,[†] and Xia Wei[†]

[†]Energy Institute, City University of New York, New York, New York 10031, United States

[‡]National Synchrotron Light Source - II, Brookhaven National Laboratory, Upton, New York 11973, United States

Supporting Information

ABSTRACT: Zinc alkaline anodes command significant share of consumer battery markets and are a key technology for the emerging grid-scale battery market. Improved understanding of this electrode is required for long-cycle deployments at kWh and MWh scale due to strict requirements on performance, cost, and safety. Here we give a modern literature survey of zinc alkaline anodes with levelized performance metrics and also present an experimental assessment of leading formulations. Long-cycle materials characterization, performance metrics, and failure analysis are reported for over 25 unique anode formulations with up to 1500 cycles and ∼1.5 years of shelf life per test. Statistical repeatability of these measurements is made for a baseline design (fewest additives) via 15 duplicates. Baseline design capacity density is 38 mAh per mL of anode volume, and lifetime throughput is 72 Ah per mL of anode volume. We then report identical measurements for anodes with improved material properties via additives and other perturbations, some of which achieve capacity density over 192 mAh per mL of anode volume and lifetime throughput of 190 Ah per mL of anode volume. Novel in operando X-ray microscopy of a cycling zinc paste anode reveals the formation of a nanoscale zinc material that cycles electrochemically and replaces the original anode structure over long-cycle life. Ex situ elemental mapping and other materials characterization suggest that the key physical processes are hydrogen evolution reaction (HER), growth of zinc oxide nanoscale material, concentration deficits of OH^- and $ZnOH_4^{2-}$, and electrodeposition of Zn growths outside and through separator membranes.

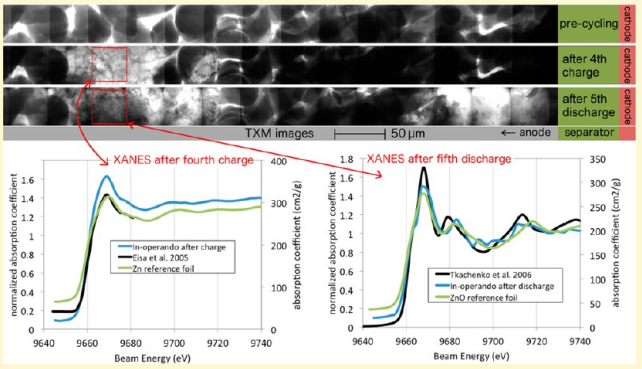

INTRODUCTION

Energy storage technology is expanding due to new applications with grid services, private homes, and microgrids. Nationally, GWh deployment of energy storage is necessary for the coming decade to stabilize the grid-penetration of wind and solar power.[1,2] Market analysis suggests that economically viable price points for energy storage range from $30−$500 per kWh depending on the specific application.[3] Fire safety is often a deal breaker, particularly in household locations, in dense urban environments, or near grid substation equipment. Lithium-ion technology remains a fire hazard,[4−6] which prohibits its use in some locations. It also has a price unlikely to fall below $200 per kWh,[7] which limits its return-on-investment for many applications. Lead acid has poor cycle-life and a slow charge/discharge rate, making it a costly option. Alternative technologies are therefore in development, including much recent work with Zn, for example, Zn intercalation cathodes,[8] novel Ni cathodes for NiZn cells,[9] shallow-cycle Mn cathodes for MnZn cells,[10] high capacity Mn cathodes for MnZn cells,[11,12] and flow-assisted Zn technologies.[13,14] Several zinc-based battery startup companies are currently underway, and many recent high-profile publications utilize Zn anodes.[8,9,11,12,14,15]

Reviews of zinc alkaline electrodes by McLarnon and Cairns[16] and Bass et al.[17] form a database for design variations as known in the late 1980s, but they give scant performance appraisal. More recent reviews[18−20] leave out most of the literature and do not compare performance with a rigorous levelized metric. Commercial and academic interest now warrants a new and thorough literature survey and a levelized performance comparison of all known designs. Therefore, we here assess known technologies by levelized and industrially relevant metrics and report a long-cycle testing program to validate the technologies and discover new ones. The metrics focus on cycle life and capacity density.

Table 1 presents the literature review and performance comparison. It includes only studies that reported cycle testing and mostly excludes technologies that use Hg or Cd due to the impracticality of using these additives under modern

Received: February 22, 2017
Revised: May 2, 2017
Published: May 3, 2017

DOI: 10.1021/acs.chemmater.7b00754
Chem. Mater. 2017, 29, 4819−4832

Table 1. Survey of Rechargeable Alkaline Zn Technologies That Mostly Avoid Use of Hg, in Chronological Order Beginning with Mid-1970s Technologies

ref	materials comprising the anode	mL electrolyte per Ah cycled	cycle life[a]	mAh cycled per gram of anode mixture[b]	mAh cycled per mL of anode volume[c]	lifetime[d] Ah discharged per mL of anode volume
21	Zn powder with 5−55% fluoride salt (either KF or NaF) in electrolyte	n.d.[e]	200	∼350	--[e]	--[e]
22	∼99% ZnO paste with ∼1% of Tl, Pb, Hg, Cd, In, or Ga, no binder, 42% KOH	∼10	>32	∼250[f]	>500[e,f]	--[e,f]
23, 24	electrolyte contains ∼5 parts K_3BO_3, K_3PO_4, K_3AsO_4, or KF to 1 part KOH	--[e]	--[e]	--[e]	--[e]	--[e]
25, 26	72% ZnO, 4% CdO, 1% PbO, 1% TiO, 2% PTFE, and 20% of either ZnF or $ZnTiO_3$	--[e]	--[e]	--[e]	--[e]	--[e]
27	91% ZnO, 5% acetylene black, 2% HgO, 1% PTFE, 1% CMC, 6.9 M KOH	∼10	∼50	112	338	17
28	68.5% ZnO, 8.6% Zn, 8.6% Bi_2O_3, 9.4% $Ca(OH)_4$, 4.9% Teflon binder	∼10	300	128	330	99
29	40% Zn−Hg amlgm; 3% starch; 6% MgO; 10% Cu-pwdr; 7% Carbowax; 35% KOH	∼15	100	127	259	26
30	94% ZnO, 2% PbO, 4% PTFE, 15% KOH with 15% KF or 22% K_3BO_3 with 1% Li_2BO_3	∼30	130	142	242	31
31	57% ZnO, 38% Ca(OH)2, 3.4%Pb3O4, 1.4% newsprint, 20% KOH	∼10	200	123	291	58
32	56% ZnO, 39% Ca(OH)2, 3.9%Pb3O4, 1.1% newsprint, 30% KOH	∼20	300	125	364	110
33	62.9% ZnO; 32.7% Ca(OH)2; 3.3% Pb3O4; 1.1% superwettable PP; 20% KOH	∼20	500	91	225	112
34, 35	71.5% ZnO, 21.5% $Ca(OH)_2$, 2% PbO, 5% PTFE, 31% KOH, 1% LiOH, sat'd ZnO	∼30	120	118	168	20
36	Zn, ZnO_polymer coatings, PTFE	150	50	11	41	2
37	64.5% ZnO; 25% $Ca(OH)_2$, 8% PbO, 2.5% PTFE binder	∼10	450	218	396	178
38	∼85% ZnO, ∼5% PTFE, 10% cellulose fibers	n.d.	175	n.d.	246	43
39	93% ZnO, 2% PbO, 4% PTFE, 1% newsprint, 4 M KOH, 2 M KF, 2 M K_2CO_3, LiOH	∼20	380	170	340	131
40	40% calcium zincate, 50% ZnO, 10% $Ca(OH)_2$	∼10	170	164	186	32
41	90% calcium zincate, 8% PTFE; 2% PbO; 4 M KOH sat'd with ZnO	n.d.[k]	400[f]	174[f]	428[f,g]	160[f,g]
42	62% ZnO, 27% $Ca(OH)_2$, 10% Bi_2O_3, ∼1% PVA binder	∼50	100	127[h]	498[h]	50[h]
43	90% Barium zincate; 10% Bi; 5 M KOH sat'd with ZnO	∼50	30	192	403	12
44, 45	∼90% ZnO, ∼5% Bi_2O_3, 1.5% binder, ∼3% fluoride salt (e.g., NaF or KF)	660	∼400[e]	--[e]	--[e]	--[e]
46	80% Ca−Zn; 5% Zn powder; 10% acetylene black, 5% PTFE, 6 M KOH sat'd ZnO	n.d.	230	240[i]	390[i]	88[i]
13, 47	37% KOH, 0.75 g/L zincate, electrodeposition from electrolyte	38	3500	125	29	103
48	80% ZnO coated in polypyrrole, 10% acetylene black, 10% PVA, 33% KOH	n.d.	70	200	588	41
49−51	hyper-dendritic zinc, ∼6 M KOH	flooded[j]	∼100	--[j]	--[j]	--[j]
10, this work	85% Zn, 10% ZnO, 5% PTFE	45	2000	11	38	72
52, 53	85% ZnAl-X-LDH, 10% acetylene black, 5% PTFE, 6 M KOH sat'd with ZnO,	n.d.[k,h]	800	200[k,h]	242[k,h]	193[k,h]
54	zinc sponge in 6 M KOH	n.d.[l]	>40	∼100[l]	∼600[l]	>24[l]
55	6 M KOH sat'd with ZnO; electrodeposition on "backside" of current collector	n.d.[l]	800	∼50[m]	31[m]	25[m]
119	zinc sponge with 11 wt % $Ca(OH)_2$ in 6 M KOH solution with 1 M LiOH	n.d.[l]	∼80	∼250[l]	∼600[l]	48[l]
this work	64.5% ZnO, 25% $Ca(OH)_2$, 8% Bi_2O_3, 2.5% Teflon binder, 25% KOH	13	990	58	192	192

[a]Cycle life was defined as the number of cycles until capacity drops below 75% of the average capacity or until Coulombic efficiency drops below 75%. Many publications that reported low capacity (<20 mAh/mL) was not included. [b]Cycle-average discharge capacity divided by grams of paste including binders, additives, and electrolyte—ignoring current collector. [c]Cycle-average mAh discharge capacity, divided by total volume necessary (including excess electrolyte) for the anode to operate. [d]Multiplication of the mAh/mL and cycle life columns gives lifetime Coulombic output per volume required for the anode. [e]These publications did not disclose sufficient information to calculate any rigorous performance metric. [f]They did not measure cycle life. They saw Pb and Tl to improve gassing rate and shape change in cells purposefully dissected after 32 cycles. [g]Approximately half of their calcium zincate exists as $Ca(OH)_2$ and ZnO. They get Coulombic efficiency near 75% for their initial cycles, and it drops to 72% by cycle 500; therefore, we list this technology as capable of 400 cycles. [h]Zhang et al.'s cell contained unrealistic excess of electrolyte, which warped their results. See Figure S25 of Supporting Information. [i]The cyclic voltammograms and chronopotentiometry charge curves suggest ref 10's active material was not calcium zincate. Instead, their evidence suggests zincate from their electrolyte was plating and deplating from the electrode surface as zinc metal. [j]Insufficient information exists in refs 49−51 to calculate mAh/mL, mAh/g, or mAh/cm^2 because porosity of the hyper-dendritic foam was not given, nor was the electrode size, charge density (mAh cycled per cm^2 of electrode area), or electrolyte volume. [k]Likely operated in excess electrolyte (>100 mL per mAh cycled) such that Zn^0 electrodeposition could be the dominant active material. [l]Did not clearly report anode thickness, porosity, or excess electrolyte. Porosity was estimated using available information in the paper. [m]Only 1 mAh cm^{-2} was tested, which is ∼15-times lower than a realistic battery. Backside plating from zincate solution requires extra volume for adequate mass transfer and for the low solubility of zincate in 6 M KOH. The practicality of backside plating is dubious.

governmental regulations. The key performance metrics are (i) discharge capacity density (mAh per mL), (ii) discharge specific capacity density (mAh per gram), and (iii) lifetime total discharge capacity (Ah per mL), where mL and gram include all components of the anode, excluding the current collector, but including electrolyte used to operate the anode in each technology disclosure, for example, excess electrolyte enables room for dendritic structures or backside plating, and allows $ZnOH_4^{2-}$ to form instead of zinc oxides. Cost per mAh and shelf life should be additional metrics but are not listed here because such data are so scarce in the literature.

A graphical representation of the data from Table 1 is shown in Figure 1, alongside performance data from commercial lead acid batteries[56] and cycle life of commercial designs of lithium-ion batteries based on cobalt oxide,[57] iron phosphate lithium,[58] or nickel cobalt oxide.[59] Except for lead-acid as a comparison, the data set excludes zinc anodes that use lead, mercury, or cadmium. The European Union prohibits the sale of batteries containing more than 0.0005% mercury or 0.002% cadmium by

DOI: 10.1021/acs.chemmater.7b00754
Chem. Mater. 2017, 29, 4819−4832

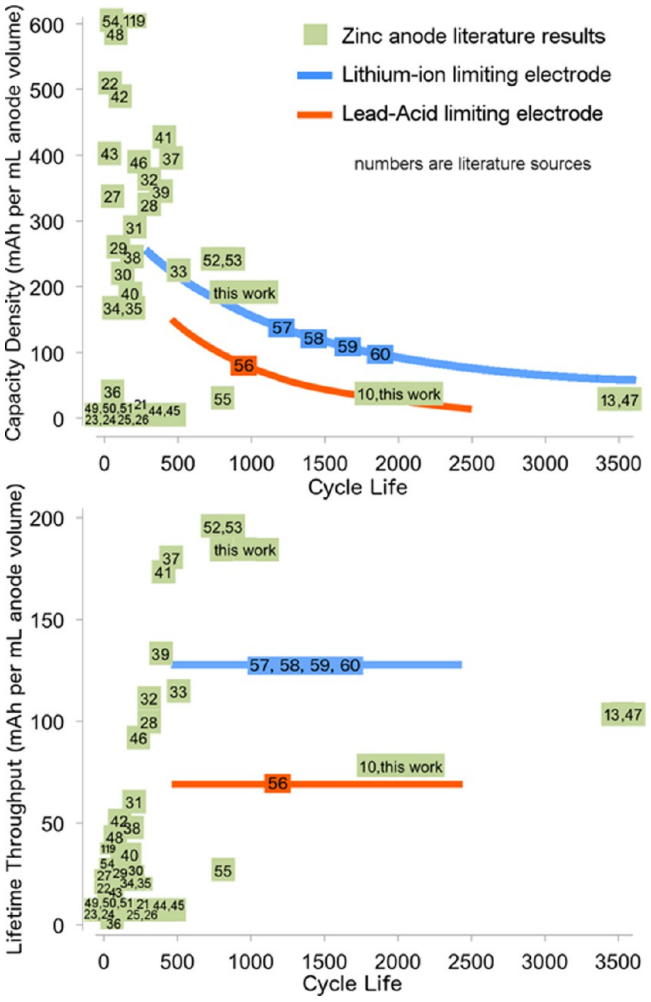

Figure 1. Mapping of performance of zinc anodes as compared to Pb-acid and Li-ion, measured by discharge capacity density (top plot) and lifetime discharge capacity (bottom plot). Orange lines are the Ah mL^{-1} capacity density of the limiting electrode in a Trojan 27-Gel 100 Ah battery.[56] Blue lines are the Ah mL^{-1} capacity density of the limiting electrode in various lithium-ion technologies.[57−60]

weight and makes all manufacturers of lead-acid batteries responsible to ensure a high percentage of their products are recycled.[61] In the United States, sale of product containing mercury compounds is banned, and concentrations in any single component may not rise above natural background concentrations.[62] Similarly, strict regulations apply to cadmium. Lead components are still in widespread use in consumer products, but restrictions exist in virtually all nations to safeguard disposal and enforce recycling. Typically the manufacturer makes an upfront financial deposit that is recovered upon product take-back from the customer. Products are classified as hazardous waste if they contain more than ∼5−100 ppm lead or if they release that concentration during leach tests.

In contrast, MnZn batteries have no toxic components, which allows users to discard them in common household waste and aids their dominance of the disposable consumer battery market. Here we focus on performance measurements of the zinc anode coupled with an Mn cathode because Mn cathodes are recently finding encouraging results,[9−11,63,64] but additional motivation comes from the use of zinc anodes in NiZn and Zn-air cells as well.[8,12−14]

EXPERIMENTAL SECTION

Electrode and Cell Fabrication. In all experiments, the cell box comprised two rectangular plates of PMMA that enclosed the electrodes as shown in Figure S1 of the Supporting Information. The cell perimeter was sealed with a rectangular wall of PMMA and Devcon gel epoxy (#14265). A zinc wire reference electrode (2 mm diameter) was flush-mounted on the inside wall of every cell through a 2 mm hole drilled through the side of each PMMA plate at a height ∼6 mm above the electrodes and ∼6 mm below the electrolyte−air interface. Zinc is experimentally well established to be a reliable reference electrode in strong KOH solution.[48,54,55,65−68] Each cell was completely sealed except for two small vent tubes (ID 700 μm, 3 cm length) in the cell top.

All cells contained three anodes and two cathodes. All electrodes were 2 in. wide, 3 in. tall, and had thickness ranging from 0.5−1.0 mm depending on the type of anode used. Unless noted otherwise, all cathodes were made the same, that is, a mix of 65% Tronox electrolytic MnO_2 with 30% KS44 carbon powder and 5% colloidal Teflon binder, pressed at 40 tons, producing a ∼6.3 g cathode with 0.7 mm thickness and porosity near 25%. This cathode was chosen to comply with recent interest in low-cost fire-safe Mn batteries[9−11,64,69] and other aqueous batteries that mate with zinc anodes[8,11−13] Three layers of cellophane were wrapped around each cathode. Discharge capacity of each cathode was ∼0.34 Wh, chosen to be 10% of 1 e^- per Mn atom, which is within the reversible portion of MnO_2 discharge. The cathode's Coulombic efficiency is near 99%, while its energy efficiency is discussed in the Results and Discussion section. Further details of the cathode are found in a prior paper.[10]

The baseline anode paste formulation was 85% w/w Zn powder (Umicore 99.9+%, ∼75 μm diameter, 030−002−00−1, 100 ppm bismuth, 200 ppm indium), 10% ZnO powder (Umicore 99%, 030−013−00−7, <1 μm diameter), 5% PTFE as colloidal solution, a 2 × 3 in^2 nickel mesh current collector (150 μm thick), and one wrap of pellon nonwoven membrane (Freudenberg, model FS2192−11SG). Nickel current collector was chosen to avoid dissolution during long-term shape change and cycle life and is not an uncommon choice in the literature.[47,49,70] This baseline anode design was the result of conversations from battery industry veterans[71] and is considered a state-of-the-art design for a long-cycle zinc anode.

The electrodes were pressed tightly together between the PMMA sheets at an initial pressure of 1500 Pa. The cellophane separators extended ∼6 mm above the electrodes. The cells were designed to have very minimal electrolyte surrounding the electrodes, ∼2 mL of electrolyte per mL of anode volume, similar to a real world industrial design. Electrolyte was filled above the electrodes by ∼1.2 cm, but only 2 mm of electrolyte existed around the electrodes' sides; 45% KOH solution was used for electrolyte.

Close to 50 such cells were made for this investigation, with formulations shown in Table 2. This includes a set of 15 identical "baseline design" cells (labeled BD01−BD15) to determine the ensemble statistics of the baseline performance. Table 2 shows an additional 25 cells (ID01−ID25) that were fabricated with a single "improvement" compared to the baseline design, for example, a single perturbation to the anode paste, separator, or electrolyte. Another eight cells were fabricated to have multiple improvements (MI01−MI08) compared to the baseline.

Unless otherwise noted, fabrication of the anode and cathode paste was achieved by the following sequence: mixing the powder components in a planetary mixer with binder and dispersant (isopropanol, mineral spirit, or water depending on the powders), roll-casting the mix into 30 × 15 cm^2 sheets of 2 mm thickness, cutting into 2 × 3 in^2 rectangles, and pressing onto a current collector at 40 tons pressure between squares of cellulose paper (LabX 123 1212.30) to prevent sticking to the press mold. Final thickness ranged from 0.5−1.0 mm. When carbon fibers or pore-formers were used, the paste was trowel-cast onto the collector instead of rolled and pressed, which increased thickness to 1.0 mm.

Materials Characterization, Cycle-Testing, Performance Metrics, and Dissection Methods. Before cycling, the material

DOI: 10.1021/acs.chemmater.7b00754
Chem. Mater. 2017, 29, 4819−4832

Table 2. Anode Designs Cycle-Tested in This Work[a]

ID	description	purpose
BD	15 identical baseline design cells, labeled BD01−BD15	establish the ensemble statistics
ID01	ammonium carbonate pore formers, graphite powder	increase permeability
ID02	duplicate of the above	duplicate
ID03	carbon fibers (~700 μm length, 10 μm diameter)	increase conductivity, permeability
ID04	duplicate of the above	duplicate
ID05	PVA binder	increase wettability
ID06	PVA-CMC binder	increase wettability
ID07	copper current collector	reduce HER
ID08	Freudenberg GK22480−100L pellon	increase wettability
ID09	Nafion separator	retain zinc
ID10	sodium citrate additive	reduce HER
ID11	duplicate of the above	duplicate
ID12	PEG200 additive (10 ppm)	reduce HER, shape change
ID13	calcium hydroxide solid powder additive to zinc paste	reduce Zn solubility, shape change
ID14	duplicate of the above	duplicate
ID15	wrapped anode in cellophane	reduce Zn migration
ID16	Freudenberg WR89−4−4 pellon	wettability, Zn migration
ID17	advanced pellon separator WR89−4−4	duplicate
ID18	carbon nanotubes 7% w/w	increase conductivity
ID19	carbon nanotubes 2% w/w	duplicate
ID20	20 mM PEG200	reduce HER, shape change
ID21	10 mM PEG200	reduce HER, shape change
ID22−ID24	deeper depth of cycling tests	deeper depth of cycling tests
ID25	64.5% ZnO, 25% $Ca(OH)_2$, 8% Bi_2O_3, and 2.5% PTFE binder	improve cycle life at high DOD
MI01	$Ca(OH)_2$ additive, PVA-CMC binder, NH_4-$2CO_3$ pore formers	multiple improvements
MI02	PVA-coated-pellon, wrap in cellophane, Cu collector	multiple improvements
MI03	duplicate of the above	multiple improvements
MI04	GK22480 pellon, C-fibers, wrap in cellophane, Cu collector	multiple improvements
MI05	duplicate of the above	multiple improvements
MI06	3% C-nanotubes, Bi_2O_3 and $Ca(OH)_2$, Cu collector, PVA binder	multiple improvements

[a]BD denotes baseline design (85% Zn, 10% ZnO, 5% PTFE, with 45% KOH). ID denotes "improved design", that is, a single perturbation to the baseline. MI denotes "multiple improvements", that is, multiple changes to the baseline.

properties of each anode formulation were characterized. Porosity was measured via mercury porosimetry. Hydraulic permeability was measured via water flux at 3 kPa hydraulic pressure across the electrode. Tortuosity was measured by diffusive flux of O_2 through the pore pathways of a dry anode. Electrical resistivity was measured via a four-point probe on paste without the current collector by using the relation $\rho = \pi V t_{th}/(i \ln[2])$. Wettability was measured by the time-rate-of-change of contact angle of a droplet of deionized water. The separator permeability was measured by salt flux across the membrane while it was held between two stirred solutions.

All cycling tests were performed on an Arbin BT-2000 48-channel battery tester. Cycling occurred galvanostatically at a rate of 10% of 1 e^- per Mn atom per hour, which equated to ~6.5 mA cm^{-2}, until 10.5% of 1 e^- per Mn atom was charged (11.9 mAh g^{-1} anode). Charging switched to potentiostatic at a cell voltage of 1.65 V. Only cells ID22−ID25 were charged differently due to their higher capacity. Discharge occurred galvanostatically at the same rate as charge until 10% of 1 e^- per Mn atom was discharged (11.4 mAh g^{-1} anode). Deeper depth of cycling was also tested as described in the Results and Discussion section. Cell failure was defined by (a) cell voltage falling below 0.8 V, (b) cycle Coulombic efficiency falling below 80%, or (c) cycle energy efficiency falling below 70%. However, cell energy efficiency and Coulombic efficiency are not appropriate metrics for studying the anode. To specifically measure the anode's performance, we recorded the anode's overvoltage as a function of time $\eta_a(t)$, which allows calculation of the energy wasted on anode overvoltage during a charge−discharge cycle:

$$\xi_a = \int_{t_{begin}}^{t_{end}} \eta_a i \, dt \quad (1)$$

where i is current, t is time, t_{begin} is the time at the beginning of a cycle, and t_{end} is the time at the end of a cycle. This wasted energy on anode overvoltage is here called "anode energy loss" (symbolized by ξ_a). The value of ξ_a includes ohmic, kinetic, and concentration overvoltage at the anode. A perfectly reversible anode will have $\xi_a = 0$ Wh. The value of ξ_a can be nondimensionalized by the cell's discharge capacity to create the "anode energy efficiency" (symbolized by Ξ_a), which is similar to the commonly used cell energy efficiency (Ξ_{cell}). Analogous metrics are established for the cathode's energy loss due to overvoltages (ξ_c) and cathode energy efficiency (Ξ_c). Cell energy efficiency (Ξ_{cell}) is equal to $1 - (\xi_a + \xi_c)/C_{cell}$ and also to $(\Xi_a + \Xi_c)$, where C_{cell} is the cell's discharge capacity.

Gas generation rate was measured in 3 min increments by completely sealing the cell and directing the only gas outlet to a micro-U-manometer filled with water. The change of liquid height on one side of the micro-U-manometer during ~3 min intervals gave measurement of the gas generation rate. The system's gas seal was assured by making the measurement with ±500 gage Pa inside the cell, and only trusting measurements that were invariant to the pressure inside the cell.

The electrolyte pH and zincate concentration were measured by collecting 0.5 mL samples from the middle of the anodes during discharge. Titrations were performed with phenolphthalein and EDTA, respectively.

Several cells were purposefully dissected and their anode materials characterized. Notably, a cell at cycle 452 and another at 914 were dissected. Most failed cells were also dissected for post-mortem materials analysis, characterized for anode and membrane properties, and investigated for failure mechanism. Dissection involved quickly disassembling and then soaking of all components in baths of

DOI: 10.1021/acs.chemmater.7b00754
Chem. Mater. 2017, 29, 4819−4832

methanol or deionized water for several days. Anodes were sliced into quarters and used for various materials measurement techniques as described in Figure S24.

In Operando X-ray Imaging and XANES. To illuminate the chemical processes leading to capacity degradation, we performed microscopy in operando with ~10 μm resolution via transmission X-ray microscopy (TXM) at the X8C beamline of NSLS at Brookhaven National Laboratory. To facilitate the in operando measurements, a paste anode of dimensions 7 mm × 0.9 mm × 0.09 mm was made with our baseline formulation, except the metallic zinc powder was sieved to include only <50 μm diameter particles. A NiOOH paste acted as the cathode. The same pellon and cellophane membranes were used. These materials were put in a specially constructed in operando cell (Figure 2), which was cycled at 10% depth of discharge of the zinc's

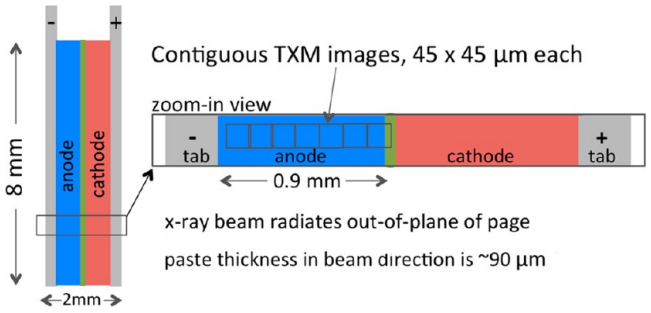

Figure 2. Schematic of the in operando X-ray transmission microscopy cell.

theoretical capacity, while the TXM images were gathered at beam energy of 9680 eV. XANES was performed at the Zn absorption edge, every few cycles, thus allowing measurements of anode Zn oxidation properties. A 40 × 40 μm^2 interrogation region was used for XANES analysis.

RESULTS AND DISCUSSION

Material Properties of Noncycled Electrodes. Table 3 gives the material characteristics of the baseline anode before cycling. The measurements of Table 3 gain significance when compared to the improved material properties of Table 4 and when compared to the material properties of baseline anodes postcycling. Figure 3 shows a cross-sectional SEM and X-ray EDS mapping of the baseline anode before cycling. An EDS mapping of fluorine (Figure S3) shows the PTFE binder to be well mixed with the ZnO powder and to fill in most pore spaces. Table 3 shows PTFE to give the anode paste poor wettability (hydrophobicity) and to increase tortuosity to 17, which is quite high compared to dense-packing of spheres that have tortuosity near 2.5.

Material properties of the improved-design (ID) anodes (precycling) are shown in Table 4. The strategy of each cell in Table 4 was to improve a single material property (precycled) compared to the baseline's material properties (precycled) and then to test all of the improvements individually with long-term cycling.

Results of Cycling the Anodes. Cell design and cycling were made similar to practical real-world batteries, as described in the Experimental Section. Time series measurements of each cell's voltage, current, and electrode overvoltage were monitored once per second, stored once per minute, and were processed hourly into charts of ξ_a, ξ_c, Ξ_a, Ξ_c, Ξ_{cell}, and cell Coulombic efficiency, all by automated computer scripts. The cells were visually inspected once per week. Purposeful dissections occurred at specific cycles and immediately after failure.

The complexity of the results obtained from cycling the anodes requires background explanation. In the simplest case of a single zinc surface exposed to a semi-infinite bath of 9 M KOH solution, plentiful evidence points to $Zn(OH)_4^{2-}$ as the predominant soluble complex,[72−74] which means the overall reaction is

$$Zn + 4OH^- \rightleftharpoons Zn(OH)_4^{2-} + 2e^- \quad (2)$$

Moderate consensus has been achieved[66,75−79] for describing the multistep reaction pathway between Zn and $Zn(OH)_4^{2-}$, which is

$$Zn + OH^- \rightleftharpoons ZnOH + e^- \quad (3)$$

$$ZnOH + OH^- \rightleftharpoons Zn(OH)_2^- \quad (4)$$

$$Zn(OH)_2^- + OH^- \rightleftharpoons Zn(OH)_3^- + e^- \text{ (suggested rds)} \quad (5)$$

$$Zn(OH)_3^- + OH^- \rightleftharpoons Zn(OH)_4^{2-} \quad (6)$$

However, real anode operation is complicated by other phenomena that occur simultaneously, that is, other Zn complexes that are thermodynamically preferred over $Zn(OH)_4^{2-}$ when the OH^- concentration drops below pH 13.5[80,81] or when Zn^{2+} supersaturation produces exotic Zn soluble complexes[82−84] or solid zinc oxides/hydroxides.

Table 3. Precycling Properties of the Baseline Anode

metric	average	standard deviation of the measurements
porosity	26%	±6% at 15% confidence interval
gas permeability	0.53 milliDarcy	±0.1 milliDarcy at 15% confidence interval
tortuosity, pressed at 40 ton	17	±3.2 at 15% confidence interval
tortuosity, unpressed	4	±1 at 15% confidence interval
wettability, initial contact angle	125°	±8° variability
wettability, rate of change of contact angle	−0.08° min^{-1}	±3.6° per minute
$Zn(OH)_4^{2-}$ in pores during discharge	1.77 mol/L, 115.2 g/L	±15 g/L at 15% confidence interval
Gas generation rate during fifth cycle	0.0045 mL/min	average of two measurements, ±0.005
4-point probe resistivity (no current collector)	5 × 10^6 Ω cm	±75% spatial variability
cellophane permeability to $Zn(OH)_4^{2-}$	3.75 × 10^{-12} m^2/s	±15% standard deviation
Pellon permeability to $Zn(OH)_4^{2-}$	1.2 × 10^{-10} m^2/s	±3 × 10^{-13} m^2/s
cellophane permeability to OH^-	above detection limit	n.a.
Pellon permeability to OH^-	9.2 × 10^{-11} m^2 s^{-1}	±15% standard deviation
ZnO precipitated in membrane	0.47 mg cm^{-2}	±20% standard deviation

DOI: 10.1021/acs.chemmater.7b00754
Chem. Mater. 2017, 29, 4819−4832

Table 4. Improved Design Anode Properties, Precycling

cell	relation to baseline
ID01, ID02	porosity: 2× higher porosity (50%)
ID03, ID04	resistivity: 1000× decrease in resistivity (~7000 Ω cm ± 50% standard deviation)
ID05, ID06	wettability: 2.5× lower contact angle (56°) and 100× increase in absorption rate
ID07	H_2 generation: 3× lower initial gas generation rate
ID08	$[Zn(OH)_4^{2-}]$ permeation through the separator: 10× reduced zincate permeability
ID08	ZnO precipitate in membrane: 2× reduction (0.19 mg cm^{-2})
ID12, ID20, ID21	H_2 generation: 2× reduction in gas generation rate
ID13, ID14	$Zn(OH)_4^{2-}$ concentration: 2× decrease in $[Zn(OH)_4^{2-}]$ (0.86 mol/L, 55.8 g/L)
ID18, ID19	resistivity: 100 000× decrease in resistivity (~20 Ω cm)

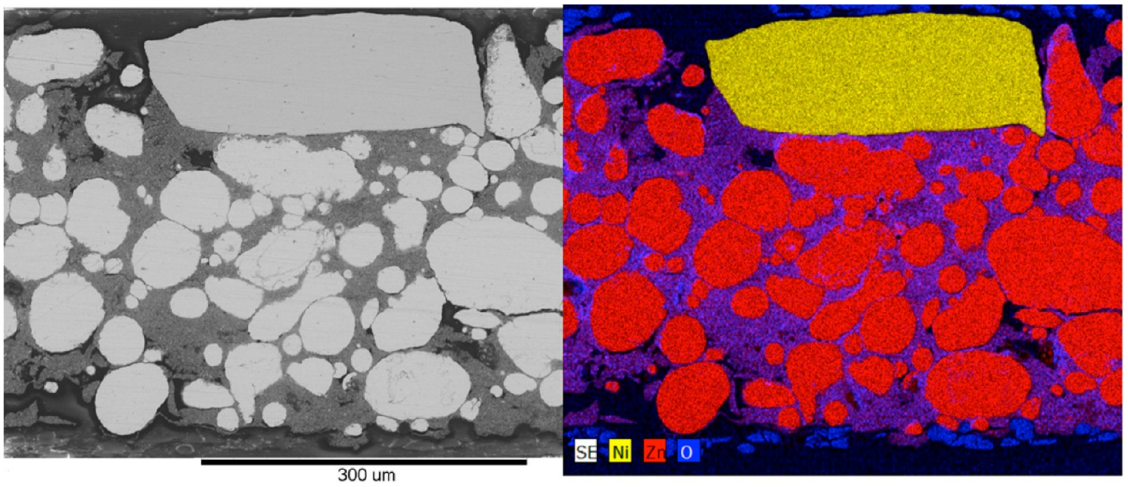

Figure 3. Backscatter SEM and EDS elemental mapping of uncycled baseline anode cross-sections. Yellow rectangle is the current collector. The entire electrode thickness (~0.5 mm) is visible.

Supersaturation occurs when mass transfer of zinc in the electrolyte is slow or when the electrolyte volume is lower than ~20 mL/mAh (solubility of zinc is ~1 M in 45% KOH solution).[63,85−88] Most industrial cells have <20 mL/mAh. Many academic publications use an abundance of electrolyte and are thus irrelevant to practical batteries. Further complexity is added by use of paste zinc electrodes, wherein tortuous pore pathways cause larger variations in ion concentration and zinc oxide chemistry.[14,89−97] Shape change becomes a final complexity when boundaries are imposed upon the edges.[13,14,98−100]

Figure 4a gives anode performance that resulted from our ensemble of 15 identical baseline design cells, and Figure 4b gives the same for the improved design anodes. The key point is not to show a breakthrough in performance, but rather to show insights into the anode material evolution on the nanoscale to microscale under practical cycling conditions. However, in a later section, we show a novel formulation of $Ca(OH)_2$ that produces "best in class" performance, which has never been reported without use of lead or mercury. Failure mechanisms in Table 5 were determined by dissection and analysis of voltage−current time series that were recorded immediately before cell death. The results show the dominant failure mechanisms are growth of anode impedance and anode zinc growths that cause short circuits.

When baseline anodes were young, that is, less than ~400 cycles, they showed anode energy loss of 0.015 Wh (i.e., $\Xi_a \approx$ 95%), which is much less than the cell's total energy loss of ~0.065 Wh (Ξ_{cell} = 80%) because of energy lost in the cathode. As cycle life exceeded 600, the baseline anode's energy loss began to grow higher, and Ξ_a began a steady decrease toward 80%, which thus caused Ξ_{cell} to decrease toward cell failure from cycle 600 to ~1200. Cell voltage during discharge is intimately connected to Ξ_{cell} because both are governed by electrode overvoltages. Cell voltage and anode overvoltage time series are given in Figure 4c and d. The anode energy metrics (ξ_a, Ξ_a) were highly correlated with cell failure. For example, when the ξ_a value for a particular cell rose above 0.05 Wh in Figure 4b, cell failure was inevitable within 100 cycles.

Ex situ material properties of many anodes were measured by dissection. After 452 cycles, cell BD09 was dissected, and the results are shown in Table 6. Compared to the precycled state, the dissections showed an increase in porosity, increase in permeability, increase in wettability, and a decrease in resistivity. Anode energy efficiency of BD09 was 93% at the time of dissection. After 914 cycles, cell BD01 was dissected, the results also given in Table 6, which showed additional increase in permeability, porosity, wettability and conductivity. In spite of the steady improvement in material properties, the anode energy efficiency dropped from ~95% (new anode) to 93% (cycle 452) and finally to 86% (cycle 914). Our dissections also found steadily growing zinc growths outside the pellon membrane of the anode (e.g., mass shown in Table 6). These Zn growths outside the membrane were rounded, metallic, globular, and grew gently through the pre-existing pore pathways of the pellon or cellophane membranes as shown in Figures S4−S7. Contrary to common thought, sharp dendrites do not occur in rechargeable zinc anodes unless the charge rate exceeds 50 mA cm^{-2} for extended time,[101] which is not typical. The rounded zinc globs grew large enough to bridge between

DOI: 10.1021/acs.chemmater.7b00754
Chem. Mater. 2017, 29, 4819−4832

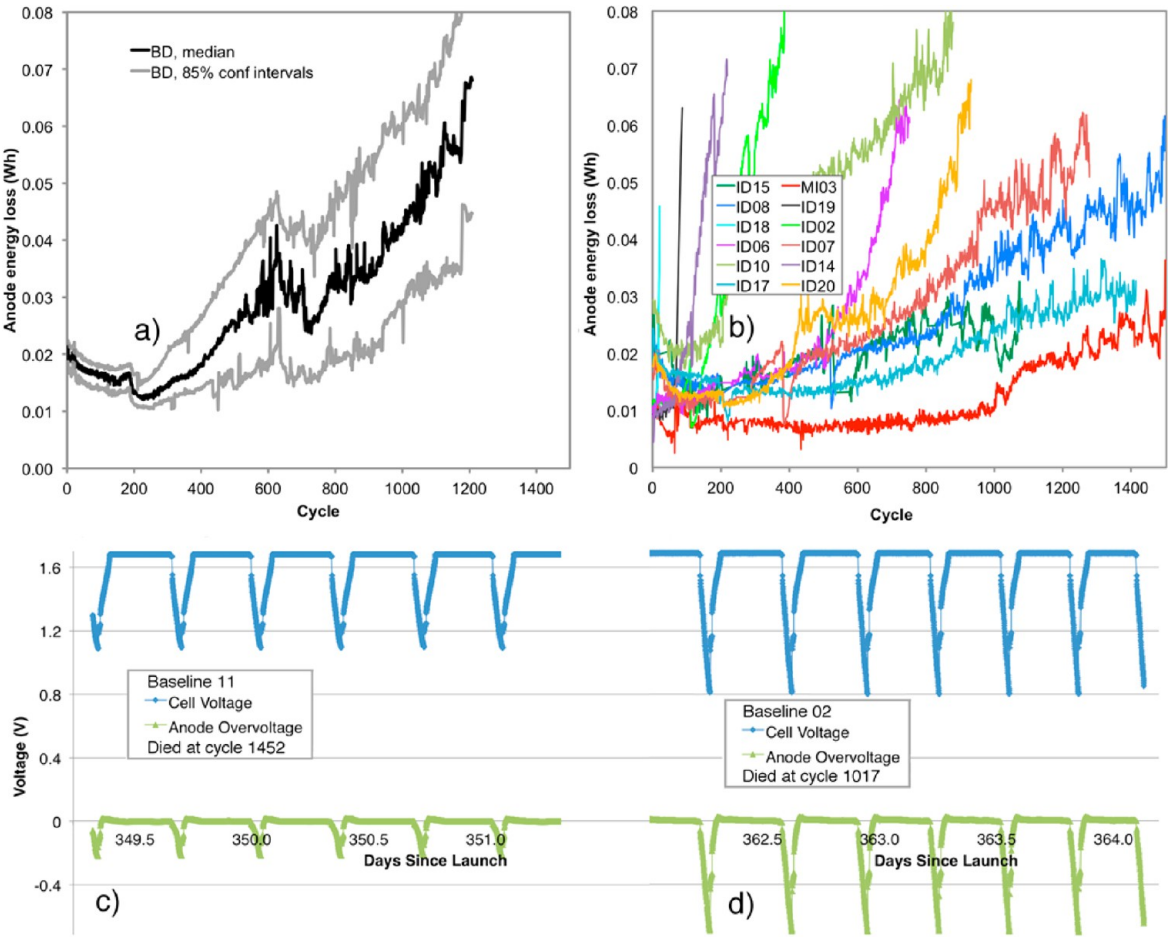

Figure 4. (a) Anode energy loss average (black line) and 85% confidence intervals (grey lines) for baseline anodes. (b) Anode energy loss of improved designs (ID). (c) Cell voltage and anode overvoltage of cell BD11 (the longest running cell) near 1000 cycles. (d) Cell voltage and anode overvoltage of cell BD02 near 1000 cycles just before it failed.

Table 5. Cycling Performance of the Baseline Anode

metric	value	measurement variability
mAh g^{-1} total anode materials	11	±4%
mAh mL^{-1} total anode volume	38	±4%
mL electrolyte per Ah capacity	45	±10%
cycle life	mean, 1216; std, 386	ensemble size of 15
shelf life during cell testing	1.5 years	±30%
Coulombic efficiency	95%	±4%
energy efficiency	80%	±4%
ξ_a, anode energy loss of a healthy cell	0.03 Wh	±30%
ξ_a, anode energy loss of a unhealthy cell	>0.09 Wh	±30%
Ξ_a, anode energy efficiency of healthy cell	96%	
Ξ_a, anode energy efficiency of unhealthy cell	<90%	
failure mech.: short circuit	5	from ensemble size of 15
failure mech.: large DC impedance	8	from ensemble size of 15
failure mech.: MnO_2 cathode problem	0	from ensemble size of 15
failure mech.: purposeful dissection	2	from ensemble size of 15

anode and cathode, to cause the short circuit failures as shown in Table 5. Careful inspection of membranes from dissected cells never found a puncture from a dendrite. Nonetheless, the soft short circuits from zinc globular growths were a significant cause of failure (Table 6). Short circuits are clearly a non-negligible occurrence in all long-cycle zinc anodes.[12,13,34,102] Soft short-circuits often go undetected and unreported because their effect on the voltage and current is subtle,[12] but over dozens of cycles they destroy electrodes and can be a dominant failure mechanism. Example time series data of voltage and current of these soft short-circuits are shown in Figure S27 and in prior work.[13]

Electron microscopy and EDS elemental mappings from cell BD01 are shown in Figure 5. Locations in the bottom half of the anode (Figure 5a,b) show similar structure to that of Figure 3, that is, original grains and original pore pathways of order

DOI: 10.1021/acs.chemmater.7b00754
Chem. Mater. 2017, 29, 4819−4832

Table 6. Properties of Dissected Anodes, Post-Cycling

metric	average	measurement variability
Cell BD09, Stopped after 452 Cycles		
permeability	5 milliDarcy	low of 0.7 to high of 11 milliDarcy
porosity	37%	±5%
wettability	initial, 71°; rate, −6° min^{-1}	n.a.
four-point resistivity: paste only	2×10^5 Ω cm	±75% spatial variability
Zn outside the Pellon membrane	250 mg	only one cell dissected
Cell BD01, Stopped after 914 Cycles		
gas permeability	30 milliDarcy	middle anode higher permeability
porosity	41%	±5%
wettability	initial, 70°; rate, −74° min^{-1}	n.a.
4-point probe resistivity: dark paste	3×10^3 ohm cm	±50% spatial variability
4-point probe resistivity: white paste	5×10^3 ohm cm	±50% spatial variability
$Zn(OH)_4^{2-}$ concentration in pores	zincate: 78 g/L	±15%
pH in pores	hydroxyls: 9 mol/L OH^-	±15%
Zn outside the Pellon membrane	1.7 g	±5%

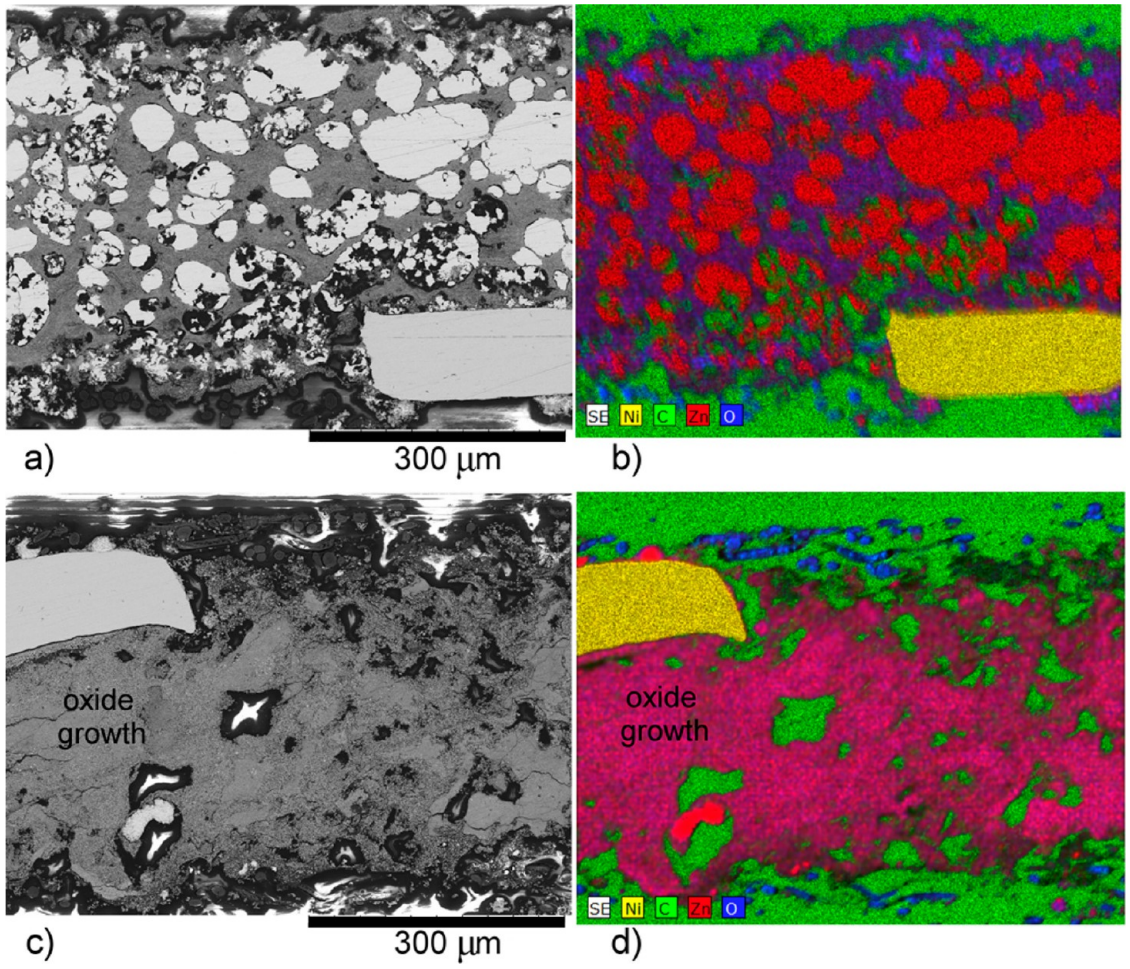

Figure 5. Cross-section dissection data from BD01 after 914 cycles. On the left are SEM backscatter electron images. On the right are corresponding EDS elemental mappings. View (a, b) from the bottom half of the anode and (c, d) from the top half of the anode. The small squares in the bottom right show that backscatter electron intensity is white/black, nickel is yellow, carbon is green, zinc is red, and oxygen is blue. The epoxy fixing agent appears in these images as green carbon material, but it was empty pore space when the anodes were in operation.

~50 μm, except pitting of the Zn grains is visible. In contrast, locations in the top half of the cycled anode (Figure 5c,d) show conversion of the original material to a nanoscale material (Figure 5c,d), which produced ex situ X-ray diffraction patterns matching a mixture of ZnO and Zn. The chemical and structural difference between top and bottom locations is likely due to density convection phenomena that affect the concentration of OH^- and $Zn(OH)_4^{2-}$ in the top versus bottom, thought to be responsible for zinc anode shape change.[99,100] The anode material from top locations had a

DOI: 10.1021/acs.chemmater.7b00754
Chem. Mater. 2017, 29, 4819−4832

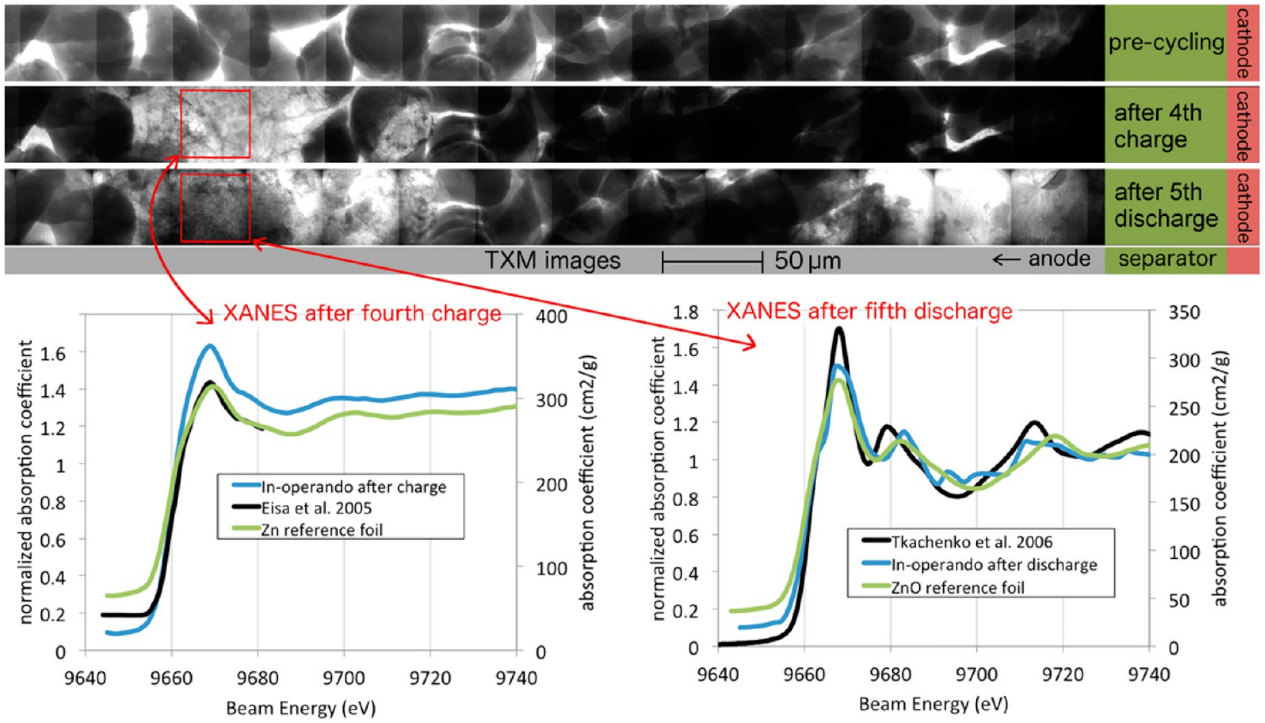

Figure 6. In operando TEM and XANES show that zinc electro-active material transforms from ~200 μm size scales down to ~100 nm size scales and participates in energy storage. XANES spectra for ZnO and $Zn(OH)_2$ are not distinguishable.

lighter color, was less bonded, and showed more electrical resistance and hydrophilicity (Table 6). Ex situ diffraction and EXAFS analysis of the nanoscale material of Figure 5c and d has rarely been reported, but existing measurements[67,85,103] suggest it to be a complicated mixture of zinc oxides and hydroxides. We explored further understanding of its formation and composition by in operando X-ray microscopy measurements.

In Operando X-ray Measurements of the Cycling Baseline Anode. Deeper understanding of the anode material evolution was obtained by in operando transmission X-ray microscopy (TXM) during three cycles at 10% DOD (data shown in Figure 6). The in operando microscopy shows new pore space is created by electrochemical dissolution of ~50 μm Zn metal grains and subsequent growth of an electro-active nanoscale material. XANES analysis was performed on an actively changing region of the nanoscale material, marked by the red square in Figure 6, after the fourth charge and again after the fifth discharge. TXM microscopy of this active region is shown with greater resolution in Figure S23. The XANES analysis confirms the material to be electrochemically cycling between two states that match XANES reference spectra for ZnO or $Zn(OH)_2$[104,105] and for Zn,[106] respectively. Spectra are shown on the bottom of Figure 6. These new data, taken together with the fact that this cell and most industrial-design cells have too small a volume of electrolyte per Ah to solubilize all the Zn^{2+} released by the anode,[88,94,107] suggest that eq 2 cannot be the total reaction. When OH^- runs low, as it inevitably does in practical zinc paste anodes, reactions are likely to proceed via an all-solid-state pathway as previously suggested for type 2 zinc oxide.[109] High surface-area nanoporous zinc material will be amenable to an all-solid-state reaction pathway because its length scales are thin enough for solid diffusion to operate. Possible all-solid-state electrochemical reactions[108−110] are

$$Zn + 2OH^- \rightleftharpoons Zn(OH)_2 + 2e^- \quad (7)$$

$$Zn + H_2O \rightleftharpoons ZnO + 2H^+ + 2e^- \quad (8)$$

where the details of the reaction pathway are a topic outside the scope of this work. Modern molecular materials analysis is needed to advance understanding of these important electrodes. Zn oxide products have wide variety (ZnO_xH_y), and the issue has not been explored sufficiently with advanced techniques.

As cycling continues into hundreds of cycles, the nanoscale zinc material expands in size and densifies, which cause the darker shade to occur in the lower red rectangle of Figure 6. This denser material fills the pore spaces and causes ion diffusion to suffer tortuous access to Zn^0 surfaces, and it also slows natural convection by increasing hydraulic resistance, which results in poor mass transfer of OH^-, K^+, and zincate. Poor mass transfer of these ions will gradually increase the presence of zinc oxide solids, increase the anode overvoltages that cause higher ξ_a (lower Ξ_a), and reduce discharge capacity. Eventually the electrode will fail due to the overvoltage. The material electrochemical evolution is a key phenomenon to the life of the anode. In operando micro- and nano-scale imaging of this process has rarely been reported.

Shape change is a related phenomenon that operates on much larger spatial scales.[86,99,100] The connection between macroscopic phenomena such as shape change and micro- and nano-scale phenomena is an outstanding problem of the materials chemistry of zinc anodes.

Improvements to the Baseline Anode Formulation. Anode energy efficiencies of the improved anode designs of Table 4 are shown in Figure 4b. Some of these anode designs were successful and others were not. For example, the KS44 powder combined with the PTFE binder in cells ID01 and ID02 created such low porosity (18%, see Figures S10−S12)

DOI: 10.1021/acs.chemmater.7b00754
Chem. Mater. 2017, 29, 4819−4832

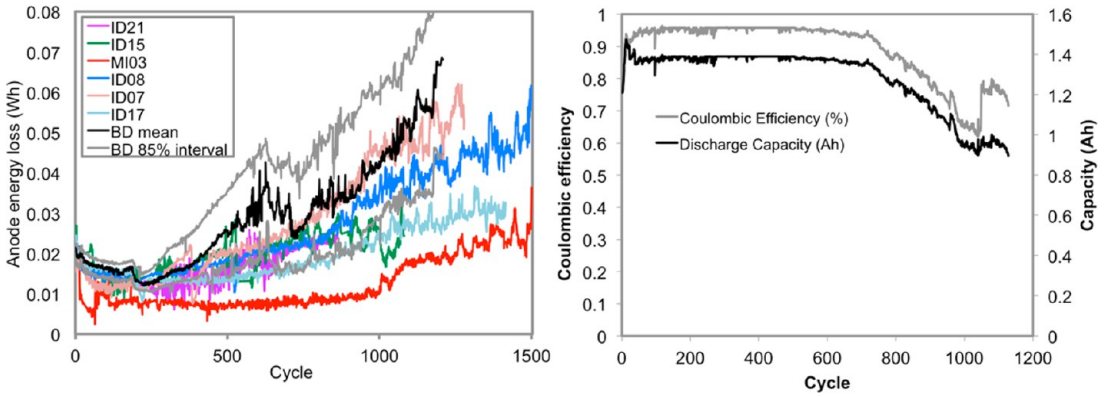

Figure 7. (a) Results from our best performing zinc anodes in the shallow DOD cycle tests. (b) Most successful formulation from the high DOD tests (ID25), which was cycled at 15% of zinc's theoretical 2 e^- capacity.

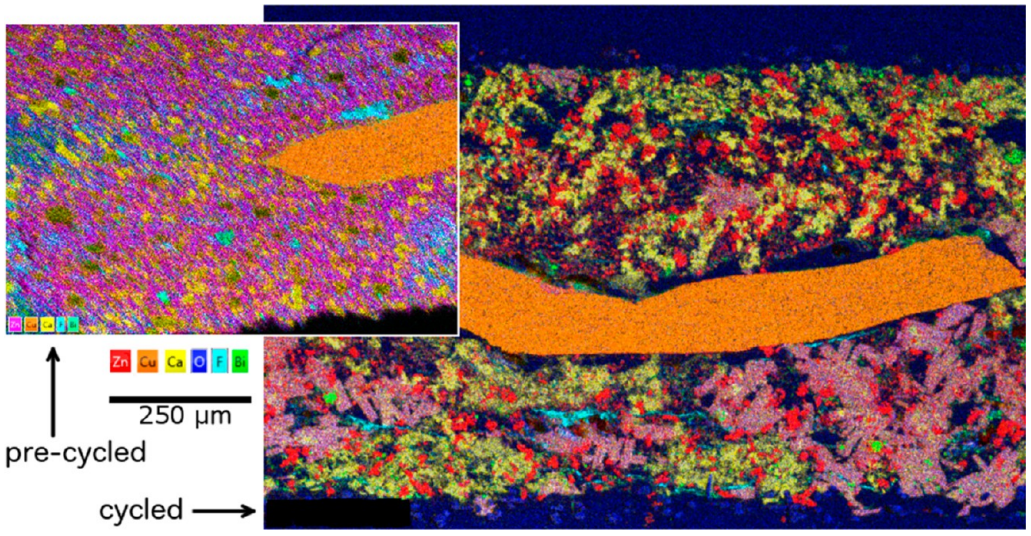

Figure 8. Cross-section SEM EDS mapping of anode from a replicated cell of ID25. On the left the anode is not-yet-cycled. On the right, the anode has undergone 25 cycles and stopped in the charged state. Additional EDS images are shown in Figure S28.

that poor ionic mass transfer and high overvoltages resulted, which led to early cell failure. Evidence for this perspective is the Zn metal remaining in the anode material after failure, which otherwise only occurs if the anode failed rapidly due to short circuits (Figures S10–S12). All other anodes that failed due to high impedance were observed to have very little Zn^0 remaining. The anodes fabricated with PVA or PVA-CMC binder (i.e., ID05 and ID06) retained a significantly darker color (i.e., Zn^0) than the baseline anodes, likely due to improved permeability of ID05 and ID06 (7.3 milliDarcy). Similarly, the amount of metallic Zn growth found outside the wrapper decreased when (i) pressure on the electrode stack was reduced, (ii) higher porosity anodes were used (Figure S2), or (iii) extra space around the electrode edges was eliminated. A possible explanation for the effect of pressure and porosity is that higher mechanical pressure on the electrode stack causes the pore spaces to collapse during discharge, thus forcing zinc metal electrodeposition to occur at the edges of the electrodes. The same explanation applies to the higher porosity anodes, since they all used lower pressure on their electrode stack.

The performances of our six most successful improved design anodes are shown in Figure 7a. The average and 85% confidence intervals of the baseline anode performance are also plotted in Figure 7a to allow determination of "significant" differences between the baseline and improved designs. Figure 7a shows that two advanced (GK22480–100L, extra fiber grafting for stronger and tighter pores) Pellon membranes (cells ID08 and ID17) were found to perform significantly better than average as well as wrapping the anode in cellophane membrane (cell ID15). Use of copper instead of nickel for the current collector in cell ID07 was found to not affect the anode energy efficiency but was found to significantly reduce gas generation (Figure S19). Use of PEG200 additive may have improved performance in cell ID21; however, this cell died early from a short circuit. Several of these improvements were combined together into cell MI03 (copper current collector, a wrap of cellophane around the anodes, and GK22480–100L Pellon), which resulted in the best anode energy efficiency of our entire study (red line of Figure 7a).

Use of carbon fibers or carbon nanotubes as additives in the anode led to early failure due to conversion of Zn^0 to ZnO, see Figure S18. It is worth noting that hydrogen evolution reaction (HER) reactions on carbons are poorly studied.[111,112] Figures S13–S18 show that Zn^0 is completely converted to ZnO when high-porosity is combined with carbon fibers, carbon nanotubes, or $Ca(OH)_2$, which was also apparent by the completely white appearance of the electrodes by visual inspection. Clearly there are many phenomena occurring simultaneously with

DOI: 10.1021/acs.chemmater.7b00754
Chem. Mater. 2017, 29, 4819–4832

these electrodes, and much scientific work remains to be performed to fully understand performance.

Higher Depth of Discharge. Cycling the baseline anode formulation at deeper depth of discharge resulted in lower cycle life as shown in Figure S26. At higher DOD, the cells failed earlier due to more rapid evolution of the material as explained in Figures 5 and 6. Additives can help avoid this early failure. Figure 7b shows successful long-cycle life of cell ID25 at 15% depth of discharge of the Zn theoretical capacity, achieved by use a few additives from Table 4 (64.5% ZnO, 25% $Ca(OH)_2$, 8% Bi_2O_3, and 2.5% PTFE binder). The performance of cell ID25 shows 990 cycles at 192 mAh per mL of anode volume (creating lifetime discharge capacity density of 190 Ah discharged per mL anode volume), which is close to the best of all literature in Table 1. Reports of similar formulations exist in the literature, but always with inclusion of PbO_2 or without cycle life performance,[28,31−35,37,40,42] and so the data of Figure 7b is considered a novel finding.

To understand the success of formulation of ID25, we collected EDS elemental mappings of cross-sections of ID25 cell replicates (Figure 8). Published literature on the effect of $Ca(OH)_2$ on zinc alkaline anodes is unclear about whether calcium zincate is an electro-active species.[31,33,41,42,113] After 25 cycles, Figure 8 shows cross-section EDS mappings of precycled and cycled anodes from replicates of ID25. These EDS mappings show that pure metallic Zn regions of ∼10 μm size form up in the cycled anode (i.e., pure red regions) and are distinguished from the precycled electrode, which contained zinc only as purple (ZnO nanopowder) regions and pink (ZnO and $Ca(OH)_2$ nanopowder mixture) regions. Yellow regions of pure $Ca(OH)_2$ appear in both precycled and cycled electrodes but are more extensive in the cycled electrode possibly due to migration of zinc away from the pink regions toward red regions. The cycled electrode was stopped after charge. Therefore, Zn is likely the major electroactive species. These findings strengthen prior explanations that the role of $Ca(OH)_2$ is simply to absorb the Zn ions from the electrolyte in a nonelectrochemical reaction. This helps the anode by keeping Zn localized near electroactive zinc metal grains. This hypothesis is further supported by our measurements of dissolved Zn concentration in electrolyte samples taken from cell ID13 (0.86 M, 56 g L^{-1}), which had $Ca(OH)_2$ added to the anode, as compared to a baseline anode (1.77 M, 115.2 g/L). Other Zn sequestering materials are also known to help such as Ga_2O_3, Ti_2O_3, $Sr(OH)_2$, Al_2O_3, or $Ba(OH)_2$.[14,37,114−117] These other sequestering materials were not tested in this work, but reports of their performance were included in constructing the literature survey of Table 1.

With regards to the bismuth added to cell ID25, bismuth is known to help zinc maintain an electric conductive pathway to the current collector[68] and also to smooth the morphology of the zinc deposits.[118]

CONCLUSIONS

Literature understanding of materials chemistry governing the performance of practical rechargeable Zn alkaline anodes is still evolving. Here we offer novel insights and formulations for long-term cycling, couched within an advanced literature review based upon a key performance metric (Ah discharged per anode volume or mass). Poor long-cycle performance of this metric is caused by the following failure mechanisms: (i) growth of rounded zinc metal deposits through pre-existing membrane pores and eventually causing short-circuits; (ii) nanoscale zinc oxide material that electrochemically cycles and overtakes the original zinc grain and pore pathway structure, eventually blocking ion mass transfer and ramping impedance high; (iii) poorly understood zinc oxide materials that appear resistant to reduction during charging; (iv) hydrogen generation that converts metallic Zn to oxides. Results from material characterization and failure analysis of 25 unique designs of zinc-paste anodes find greatest success with (i) reductions of HER activity, (ii) physically trapping the zinc material inside additional membranes or inside powder compounds such as $Ca(OH)_2$. A novel formulation achieves 990 cycles at 192 mAh per mL of total anode volume, without use of Pb or Hg, which is close to the best of all prior literature. Novel in operando X-ray microscopy on a cycling zinc anode reveals the formation of a nanoscale zinc material that remains electrochemically active and overtakes the original anode structure. Ex situ elemental mapping and other materials characterization suggest the key physical processes are HER, ZnO clogging of pore spaces, OH^- and $ZnOH_4^{2-}$ concentration deficits or supersaturation, and electrodeposition of Zn growths outside the membrane wrapper. Modern materials chemistry will be critical to advance understanding of the many simultaneous phenomena that govern the life of practical zinc paste anodes. Couplings between the molecular and macroscopic scales will be necessary.

ASSOCIATED CONTENT

Supporting Information

The Supporting Information is available free of charge on the ACS Publications website at DOI: 10.1021/acs.chemmater.7b00754.

Cell box design; additional EDS elemental mappings of cross-sections; additional SEM of cross-sections; deep cycling results; hydrotalcite preliminary results; dissection protocol (PDF)

AUTHOR INFORMATION

Corresponding Author

*E-mail: dturney@ccny.cuny.edu.

ORCID

Damon E. Turney: 0000-0003-1759-1735

Notes

The authors declare no competing financial interest.

ACKNOWLEDGMENTS

This work was supported by the U.S. Department of Energy DOE-ARPA-E Grant No. DE-AR0000150. We gratefully acknowledge data collection support from Daniel Wildman, Andres Quito, Can Erdonmez, Stoyan Bliznakov, Nilesh Ingale, Roman Yakobov, Zeeshan Saroya, and Jerome Fineman.

REFERENCES

(1) Kutscher, C. F. *Tackling Climate Change in the U.S.*; American Solar Energy Society, 2007.

(2) Midwest Independent System Operator. *Final Report: 2006 Minnesota Wind Integration Study*; Minnesota Public Utilities, 2006.

(3) Eyer, J.; Corey, G. *Energy Storage for the Electricity Grid: Benefits and Market Potential Assessment Guide, A Study for the DOE Energy Storage Systems Program, Sandia Report 2010−0815*; Sandia National Laboratory, 2010.

DOI: 10.1021/acs.chemmater.7b00754
Chem. Mater. 2017, 29, 4819−4832

(4) Larsson, F.; Andersson, P.; Blomqvist, P.; Lorén, A.; Mellander, B. E. Characteristics Of Lithium-Ion Batteries During Fire Tests. *J. Power Sources* **2014**, *271*, 414−420.
(5) Ping, P.; Wang, Q.; Huang, P.; Li, K.; Sun, J.; Kong, D.; Chen, C. Study Of the Fire Behavior Of High-Energy Lithium-Ion Batteries With Full-Scale Burning Test. *J. Power Sources* **2015**, *285*, 80−89.
(6) Wang, Q.; Ping, P.; Zhao, X.; Chu, G.; Sun, J.; Chen, C. Thermal Runaway Caused Fire And Explosion Of Lithium Ion Battery. *J. Power Sources* **2012**, *208*, 210−224.
(7) Crabtree, G.; Kócs, E.; Trahey, L. The energy-storage frontier: Lithium-ion batteries and beyond. *MRS Bull.* **2015**, *40*, 1067−1078.
(8) Kundu, D.; Adams, B. D.; Duffort, V.; Vajargah, S. H.; Nazar, L. F. A High-Capacity And Long-Life Aqueous Rechargeable Zinc Battery Using A Metal Oxide Intercalation Cathode. *Nat. Energy* **2016**, *1*, 16119.
(9) Gong, M.; Li, Y.; Zhang, H.; Zhang, B.; Zhou, W.; Feng, J.; Wang, H.; Liang, Y.; Fan, Z.; Liu, J.; Dai, H. Ultrafast high-capacity NiZn battery with NiAlCo-layered double hydroxide. *Energy Environ. Sci.* **2014**, *7*, 2025−2032.
(10) Ingale, N. D.; Gallaway, J. W.; Nyce, M.; Couzis, A.; Banerjee, S. Rechargeability and Economic Aspects of Alkaline Zinc−Manganese Dioxide Cells for Electrical Storage and Load Leveling. *J. Power Sources* **2015**, *276*, 7−18.
(11) Yadav, G.; Gallaway, J.; Turney, D. E.; Nyce, M.; Wei, X.; Huang, J.; Banerjee, S. Regenerable Cu-Intercalated MnO_2 Layered Cathode for Highly Cyclable Energy Dense Batteries. *Nat. Commun.* **2017**, *8*, 14424.
(12) Pan, H.; Shao, Y.; Yan, P.; Cheng, Y.; Han, K. S.; Nie, Z.; Wang, C.; Yang, J.; Li, X.; Bhattacharya, P.; Mueller, K. T.; Liu, J. Reversible Aqueous Zinc/Manganese Oxide Energy Storage from Conversion Reactions. *Nat. Energy* **2016**, *1*, 16039.
(13) Turney, D. E.; Shmukler, M.; Galloway, K.; Klein, M.; Ito, Y.; Sholklapper, T.; Gallaway, J. W.; Nyce, M.; Banerjee, S. Development and Testing of an Economic Grid-Scale Flow-Assisted Zinc/Nickel-Hydroxide Alkaline Battery. *J. Power Sources* **2014**, *264*, 49−58.
(14) Soloveichik, G. L. Flow Batteries: Current Status and Trends. *Chem. Rev.* **2015**, *115*, 11533−11558.
(15) Urban Electric Power, ViZn Energy Systems, Imprint Energy, EOS Energy Storage, Powergenix Systems Inc. and Fluidic Inc., Personal communication, 2014.
(16) McLarnon, F. R.; Cairns, E. J. The Secondary Alkaline Zinc Electrodes. *J. Electrochem. Soc.* **1991**, *138*, 645−664.
(17) Bass, K.; Mitchell, P. J.; Wilcox, G. D.; Smith, J. Methods for the Reduction of Shape Change and Dendritic Growth in Zinc-Based Secondary Cells. *J. Power Sources* **1991**, *35*, 333−351.
(18) Caramia, V.; Bozzini, B. Materials Science Aspects of Zinc−Air Batteries: A Review. *Mater. Renew. Sustain. Energy* **2014**, *3*, 1−12.
(19) Kim, H.; Jeong, G.; Kim, Y.-U.; Kim, J.-H.; Park, C.-M.; Sohn, H.-J. Metallic Anodes for Next Generation Secondary Batteries. *Chem. Soc. Rev.* **2013**, *42*, 9011−9034.
(20) Li, Y.; Dai, H. Recent Advances in Zinc−Air Batteries. *Chem. Soc. Rev.* **2014**, *43*, 5257−5275.
(21) Sandera, J. *Composition for a Zinc Electrode*. U.S. Patent 4017665, 1977.
(22) Himy, A.; Wagner, O.C. *Stable Alkaline Zinc Electrode*. U.S. Patent 4084047, 1978.
(23) Eisenberg, M. *Electrolyte for Zinc Anode Batteries and Method of Making Same*. U.S. Patent 4224391, 1980.
(24) Carlson, E. *Ternary Electrolyte for Secondary Electrochemical Cells*. U.S. Patent 4273841, 1981.
(25) Vaidyanathan, H. *Zinc Electrode*. U.S. Patent 4304828, 1981.
(26) Eisenberg, M. *Alkaline Galvanic Cells*. U.S. Patent 5215836, 1993.
(27) Biegler, C.; Deutscher, R. L.; Fletcher, S.; Hua, S.; Woods, R. Accelerated Testing of Additives in Zinc Plates of Nickel Zinc Cells. *J. Electrochem. Soc.* **1983**, *130*, 2303−2309.
(28) Sato, Y.; Kanda, M.; Niki, H.; Ueno, M.; Murata, K.; Shirogami, T.; Takamura, T. Long Life Sealed Nickel Zinc Cell Using a New Separator. *J. Power Sources* **1983**, *9*, 147−159.
(29) Binder, Y.; Odar, W. Experimental Survey of Rechargeable Alkaline Zinc Electrodes. *J. Power Sources* **1984**, *13*, 9−21.
(30) Nichols, J. T.; McLarnon, F. R.; Cairns, E. J. Zinc Electrode Cycle-Life Performance in Alkaline Electrolytes Having Reduced Zinc Species Solubility. *Chem. Eng. Commun.* **1985**, *38*, 357−381.
(31) Gagnon, E. G. Effects of KOH Concentration on the Shape Change and Cycle Life of Zn/NiOOH Cells. *J. Electrochem. Soc.* **1986**, *133*, 1989−1995.
(32) Jones, R. A. *Nickel-Zinc Cell*. U.S. Patent 4358517, 1982.
(33) Gagnon, E. G.; Wang, Y.-M. Pasted-Rolled Zinc Electrodes Containing Calcium Hydroxide for Use in Zn/NiOOH Cells. *J. Electrochem. Soc.* **1987**, *134*, 2091−2096.
(34) Jain, R.; McLarnon, F.; Cairns, E. J. Cycle-Life Improvement of Zn/NiOOH Cells by the Addition of $Ca(OH)_2$ to the Zinc Electrode. *Cycle-Life Improvement of Zn/NiOOH Cells by the Addition of $Ca(OH)_2$ to the Zinc Electrode, Report: LBL-25332*; Lawrence Berkeley National Laboratory, 1989.
(35) Jain, R.; Adler, T. C.; McLarnon, F. R.; Cairns, E. J. Development of Long-Lived High-Performance Zinc-Calcium/Nickel Oxide Cells. *J. Appl. Electrochem.* **1992**, *22*, 1039−1048.
(36) Suga, S. A.; Kuroda, N. *Zinc Electrode for Alkaline Storage Battery*. U.S. Patent 5348820, 1994.
(37) Charkey, A. *Sealed Zinc Secondary Battery and Zinc Electrode Therefor*. U.S. Patent 5460899, 1995.
(38) Müller, S.; Holzer, F.; Haas, O. Optimized Zinc Electrode for the Rechargeable Zinc−Air Battery. *J. Appl. Electrochem.* **1998**, *28*, 895−898.
(39) Adler, T. C.; McLarnon, F. R.; Cairns, E. J. Investigations of a New Family of Alkaline-Fluoride-Carbonate Electrolytes for Zinc/Nickel Oxide Cells. *Ind. Eng. Chem. Res.* **1998**, *37*, 3237−3241.
(40) Charkey, A. *Calcium-Zincate Electrode for Alkaline Batteries and Method for Making Same*. U.S. Patent 5863676, 1999.
(41) Yu, J.; Yang, H.; Ai, X.; Zhu, X. A Study of Calcium Zincate as Negative Electrode Materials for Secondary Batteries. *J. Power Sources* **2001**, *103*, 93−97.
(42) Zhang, C.; Wang, J. M.; Zhang, L.; Zhang, J. Q.; Cao, C. N. Study of the Performance of Secondary Alkaline Pasted Zinc Electrodes. *J. Appl. Electrochem.* **2001**, *31*, 1049−1054.
(43) Zheng, Y.; Wang, J. M.; Chen, H.; Zhang, J. Q.; Cao, C. N. Effects of Barium on the Performance of Secondary Alkaline Zinc Electrode. *Mater. Chem. Phys.* **2004**, *84*, 99−106.
(44) Phillips, J. *Alkaline Cells Having Low Toxicity Rechargeable Zinc Electrodes*. U.S. Patent 6818350, 2009.
(45) Phillips, J.; Mohanta, S.; Maske, C.; Bose, D.C.; Wu, J. J.; McKinney, B. L. *Pasted Zinc Electrode for Rechargeable Nickel-Zinc Batteries*. U.S. Patent 8501351, 2013.
(46) Wang, R.; Yang, Z.; Yang, B.; Fan, X.; Wang, T. A Novel Alcohol-Thermal Synthesis Method of Calcium Zincates Negative Electrode Materials for Ni-Zn Secondary Batteries. *J. Power Sources* **2014**, *246*, 313−321.
(47) Ito, Y.; Nyce, M.; Plivelich, R.; Klein, M.; Steingart, D.; Banerjee, S. Zinc Morphology in Zinc-Nickel Flow Assisted Batteries and Impact on Performance. *J. Power Sources* **2011**, *196*, 2340−2345.
(48) Gan, W.; Zhou, D.; Zhao, J.; Zhou, L. Stable Zinc Anodes by In Situ Polymerization of Conducting Polymer to Conformally Coat Zinc Oxide Particles. *J. Appl. Electrochem.* **2015**, *45*, 913−919.
(49) Chamoun, M.; Hertzberg, B. J.; Gupta, T.; Davies, D.; Bhadra, S.; Van Tassell, B.; Erdonmez, C.; Steingart, D. A. Hyper-Dendritic Nanoporous Zinc Foam Anodes. *NPG Asia Mater.* **2015**, *7*, e178.
(50) Davies, G.; Hsieh, A. G.; Hultmark, M.; Mueller, M. E.; Steingart, D. A. Utilization of Hyper-Dendritic Zinc During High Rate Discharge in Alkaline Electrolytes. *J. Electrochem. Soc.* **2016**, *163*, A1340−A1347.
(51) Gupta, T.; Kim, A.; Phadke, S.; Biswas, S.; Luong, T.; Hertzberg, B. J.; Chamoun, M.; Evans-Lutterodt, K.; Steingart, D. A. Improving The Cycle Life Of A High-Rate, High-Potential Aqueous Dual-Ion Battery using Hyper-Dendritic Zinc and Copper Hexacyanoferrate. *J. Power Sources* **2016**, *305*, 22−29.

DOI: 10.1021/acs.chemmater.7b00754
Chem. Mater. 2017, 29, 4819−4832

(52) Wang, R.; Yang, Z.; Yang, B.; Wang, T.; Chu, Z. Superior Cycle Stability and High Rate Capability of Zn−Al−In-Hydrotalcite as Negative Electrode Materials for Ni−Zn Secondary Batteries. *J. Power Sources* **2014**, *251*, 344−350.
(53) Zhang, Z.; Yang, Z.; Huang, J.; Feng, Z.; Xie, X. Enhancement of Electrochemical Performance with Zn-Al-Bi Layered Hydrotalcites as Anode Material for Zn/Ni Secondary Battery. *Electrochim. Acta* **2015**, *155*, 61−68.
(54) Parker, J. F.; Chervin, C. N.; Nelson, E. S.; Rolison, D. R.; Long, J. W. Wiring Zinc in Three Dimensions Re-Writes Battery Performance—Dendrite-Free Cycling. *Energy Environ. Sci.* **2014**, *7*, 1117−1124.
(55) Higashi, S.; Lee, S. W.; Lee, J. S.; Takechi, K.; Cui, Y. Avoiding Short Circuits from Zinc Metal Dendrites in Anode by Backside-Plating Configuration. *Nat. Commun.* **2016**, *7*, 11801.
(56) *100Ah Pb-Acid Battery: 27-Gel Data Sheet*; Trojan Inc., 2015.
(57) Choi, S. S.; Lim, H. S. Factors that Affect Cycle-Life and Possible Degradation Mechanisms of a Li-Ion Cell Based on $LiCoO_2$. *J. Power Sources* **2002**, *111*, 130−136.
(58) Peterson, S. B.; Apt, J.; Whitacre, J. F. Lithium-Ion Battery Cell Degradation Resulting from Realistic Vehicle and Vehicle-To-Grid Utilization. *J. Power Sources* **2010**, *195*, 2385−2392.
(59) Bloom, I.; Cole, B. W.; Sohn, J. J.; Jones, S. A.; Polzin, E. G.; Battaglia, V. S.; Henriksen, G. L.; Motloch, C.; Richardson, R.; Unkelhaeuser, T.; et al. An Accelerated Calendar and Cycle Life Study of Li-Ion Cells. *J. Power Sources* **2001**, *101*, 238−247.
(60) Ecker, M.; Nieto, N.; Käbitz, S.; Schmalstieg, J.; Blanke, H.; Warnecke, A.; Sauer, D. U. Calendar and Cycle Life Study of $Li(NiMnCo)O_2$-Based 18650 Lithium-Ion Batteries. *J. Power Sources* **2014**, *248*, 839−851.
(61) European Union. Directive 2006/66/EC of the European Parliament and of the Council of the 6 September 2006 on batteries and accumulators and repealing Directive 91/157/EEC. *Official Journal of the European Union*; European Union (L 266), 2006.
(62) Mercury-Containing and Rechargeable Battery Management Act (The Battery Act); *U.S. Public Law 104−142*; U.S. 104th Congress, 1996; pp 14301−14307.
(63) Gallaway, J. W.; Erdonmez, C. K.; Zhong, Z.; Croft, M.; Sviridov, L. A.; Sholklapper, T. Z.; Turney, D. E.; Banerjee, S.; Steingart, D. A. Real-Time Materials Evolution Visualized Within Intact Cycling Alkaline Batteries. *J. Mater. Chem. A* **2014**, *2*, 2757−2764.
(64) Gallaway, J. W.; Hertzberg, B. J.; Zhong, Z.; Croft, M.; Turney, D. E.; Yadav, G. G.; Steingart, D.; Erdonmez, C. K.; Banerjee, S. Operando Identification of the Point Of $[Mn\ 2]O_4$ Spinel Formation During Γ-MnO_2 Discharge Within Batteries. *J. Power Sources* **2016**, *321*, 135−142.
(65) Dirkse, T. P.; Hampson, N. A. The Anodic Behaviour of Zinc in Aqueous Koh Solution 0.1. Passivation Experiments at Very High Current Densities. *Electrochim. Acta* **1971**, *16*, 2049−2056.
(66) Bockris, J. O. M.; Nagy, Z.; Damjanovic, A. On the Deposition and Dissolution of Zinc in Alkaline Solutions. *J. Electrochem. Soc.* **1972**, *119*, 285−295.
(67) McBreen, J. *The Zinc Electrode in Alkaline Electrolyte, Report 61819*; Brookhaven National Laboratory, 1996.
(68) Shin, J.; You, J.-M.; Lee, J. Z.; Kumar, R.; Yin, L.; Wang, J.; Meng, Y. S. Deposition Of ZnO on Bismuth Species Towards a Rechargeable Zn-Based Aqueous Battery. *Phys. Chem. Chem. Phys.* **2016**, *18*, 26376−26382.
(69) Jiang, B.; Xu, C.; Wu, C.; Dong, L.; Li, J.; Kang, F. Manganese Sesquioxide as Cathode Material for Multivalent Zinc Ion Battery with High Capacity and Long Cycle Life. *Electrochim. Acta* **2017**, *229*, 422−429.
(70) Hampden-Smith, M.; Djokic, S.; Atanassova, P.; Bhatia, R.; Napolitano, P. *Methods and Materials for the Preparation of a Zinc Anode Useful for Batteries and Fuel Cells*. U.S. Patent US20030099882, 2001.
(71) Salkind, A. New York, NY, 2013; Klein, M. G. New York, NY, 2012; Nyce, M. Danbury, CT, 2015. Personal communications.
(72) Dirkse, T. P. The Nature of the Zinc-Containing Ion in Strongly Alkaline Solutions. *J. Electrochem. Soc.* **1954**, *101*, 328−331.
(73) Cain, K. J.; Melendres, C. A.; Maroni, V. A. Raman and ^{67}Zn NMR-Studies of the Structure of Zinc (II) Solutions in Concentrated Aqueous Potassium Hydroxide. *J. Electrochem. Soc.* **1987**, *18*, 519−524.
(74) Pandya, K. I.; Russell, A. E.; McBreen, J.; O'Grady, W. E. EXAFS Investigations Of Zn(II) In Concentrated Aqueous Hydroxide Solutions. *J. Phys. Chem.* **1995**, *99*, 11967−11973.
(75) Dirkse, T. P. The Behavior of the Zinc Electrode in Alkaline-Solutions. 2. Reaction Orders at the Equilibrium Potential. *J. Electrochem. Soc.* **1979**, *126*, 541−543.
(76) Hendrikx, J.; van der Putten, A.; Visscher, W.; Barendrecht, E. The Electrodeposition and Dissolution of Zinc And Amalgamated Zinc In Alkaline Solutions. *Electrochim. Acta* **1984**, *29*, 81−89.
(77) Chang, Y. C.; Prentice, G. A Model for the Anodic-Dissolution of Zinc in Alkaline Electrolyte - Kinetics of Initial Dissolution. *J. Electrochem. Soc.* **1984**, *131*, 1465−1468.
(78) Cachet, C.; Saidani, B.; Wiart, R. The Behavior Of Zinc Electrode In Alkaline Electrolytes 0.1. A Kinetic-Analysis Of Cathodic Deposition. *J. Electrochem. Soc.* **1991**, *138*, 678−687.
(79) Cachet, C.; Saidani, B.; Wiart, R. The Behavior of Zinc Electrode in Alkaline Electrolytes 0.2. A Kinetic-Analysis of Anodic-Dissolution. *J. Electrochem. Soc.* **1992**, *139*, 644−654.
(80) Peulon, S.; Lincot, D. Cathodic Electrodeposition from Aqueous Solution of Dense or Open-Structured Zinc Oxide Films. *J. Electrochem. Soc.* **1998**, *145*, 864−874.
(81) Martell, A. E.; Smith, B. M. *Critical Stability Constants*; Plenum Press: New York, 1976; Vol. *4*.
(82) Briggs, A. G.; Hampson, N. A.; Marshall, A. Concentrated Potassium Zincate Solutions Studied Using Laser Raman Spectroscopy and Potentiometry. *J. Chem. Soc., Faraday Trans. 2* **1974**, *70*, 1978.
(83) Debiemmechouvy, C.; Vedel, J. Supersaturated Zincate Solutions - A Study of the Decomposition Kinetics. *J. Electrochem. Soc.* **1991**, *138*, 2538−2542.
(84) Debiemmechouvy, C.; Vedel, J. Supersaturated Zincate Solutions - A Structural Study. *J. Electrochem. Soc.* **1995**, *142*, 1359−1364.
(85) Powers, R. W. Film Formation and Hydrogen Evolution on the Alkaline Zinc Electrode. *J. Electrochem. Soc.* **1971**, *118*, 685−695.
(86) Hamby, D. C.; Hoover, N. J.; Wirkkala, J.; Zahnle, D. Concentration Changes in Porous Zn Electrodes During Cycling. *J. Electrochem. Soc.* **1979**, *126*, 2110−2118.
(87) Arise, I.; Kawai, S.; Fukunaka, Y.; McLarnon, F. R. Numerical Calculation of Ionic Mass-Transfer Rates Accompanying Anodic Zinc Dissolution in Alkaline Solution. *J. Electrochem. Soc.* **2010**, *157*, A171−A178.
(88) Arise, I.; Kawai, S.; Fukunaka, Y.; McLarnon, F. R. Coupling Phenomena between Zinc Surface Morphological Variations and Ionic Mass Transfer Rate in Alkaline Solution. *J. Electrochem. Soc.* **2013**, *160*, D66−D74.
(89) Nagy, Z.; Bockris, J. O. On the Electrochemistry of Porous Zinc Electrodes in Alkaline Solutions. *J. Electrochem. Soc.* **1972**, *119*, 1129−1136.
(90) Sunu, W. G.; Bennion, D. N. Transient and Failure Analyses of the Porous Zinc Electrode I. Theoretical. *J. Electrochem. Soc.* **1980**, *127*, 2007−2016.
(91) Sunu, W. G.; Bennion, D. N. Transient and Failure Analyses of the Porous Zinc Electrode II. Experimental. *J. Electrochem. Soc.* **1980**, *127*, 2017−2025.
(92) Isaacson, M. J.; McLarnon, F. R.; Cairns, E. J. Current Density and ZnO Precipitation-Dissolution Distributions in Zn-ZnO Porous Electrodes and Their Effect on Material Redistribution: A Two-Dimensional Mathematical Model. *J. Electrochem. Soc.* **1990**, *137*, 2014−2021.
(93) Mao, Z.; White, R. E. Mathematical Modeling Of A Primary Zinc/Air Battery. *J. Electrochem. Soc.* **1992**, *139*, 1105−1114.
(94) Podlaha, E. J.; Cheh, H. Y. Modeling Of Cylindrical Alkaline Cells V. High Discharge Rates. *J. Electrochem. Soc.* **1994**, *141*, 15−27.

DOI: 10.1021/acs.chemmater.7b00754
Chem. Mater. 2017, 29, 4819−4832

(95) Horn, Q. C.; Shao-Horn, Y. Morphology and Spatial Distribution of ZnO Formed in Discharged Alkaline Zn/MnO_2 AA Cells. *J. Electrochem. Soc.* **2003**, *150*, A652−A658.
(96) Minakshi, M.; Ionescu, M. The Anodic Behavior of Planar and Porous Zinc Electrodes in Alkaline Electrolyte. *Int. J. Hydrogen Energy* **2010**, *35*, 7618−7622.
(97) Haibel, A. I.; Manke, A. I.; Melzer, A.; Banhart, J. In Situ Microtomographic Monitoring of Discharging Processes in Alkaline Cells. *J. Electrochem. Soc.* **2010**, *157*, A387−A391.
(98) McBreen, J. Zinc Electrode Shape Change in Secondary Cells. *J. Electrochem. Soc.* **1972**, *119*, 1620−1628.
(99) Einerhand, R.; Visscher, W.; de Goeij, J. J. M.; Barendrecht, E. Zinc Electrode Shape Change I. In Situ Monitoring. *J. Electrochem. Soc.* **1991**, *138*, 1−7.
(100) Einerhand, R.; Visscher, W.; de Goeij, J. J. M.; Barendrecht, E. Zinc Electrode Shape Change II. Process and Mechanism. *J. Electrochem. Soc.* **1991**, *138*, 7−17.
(101) Wang, R. Y.; Kirk, D. W.; Zhang, G. X. Effects of Deposition Conditions on the Morphology of Zinc Deposits from Alkaline Zincate Solutions. *J. Electrochem. Soc.* **2006**, *153*, C357−C364.
(102) Shen, Y.; Kordesch, K. The Mechanism of Capacity Fade of Rechargeable Alkaline Manganese Dioxide Zinc Cells. *J. Power Sources* **2000**, *87*, 162−166.
(103) Armstrong, R. D.; Bell, M. F. *The Electrochemical Behavior of Zinc in Alkaline Solution* **1974**, *4*, 1.
(104) Tkachenko, O. P.; Klementiev, K. V.; van den Berg, M. W. E.; Gies, H.; Grunert, W. The Reduction of Copper in Porous Matrices—The Role of Electrostatic Stabilisation. *Phys. Chem. Chem. Phys.* **2006**, *8*, 1539−1549.
(105) Chang, S. H.; Wei, Y. L.; Wang, H. P. Zinc Species Distribution in EDTA-Extract Residues of Zinc-Contaminated Soil. *J. Electron Spectrosc. Relat. Phenom.* **2007**, *156-158*, 220−223.
(106) Eisa, M. H.; Shen, H.; Yao, H. Y.; Mi, Y.; Zhou, Z. Y.; Hu, T. D.; Xie, Y. N. Studies on Absorption Coefficient Near Edge of Multi Elements. *J. Quant. Spectrosc. Radiat. Transfer* **2005**, *96*, 503−511.
(107) Szpak, S. The Zn-KOH System: The Solution-Precipitation Path for Anodic ZnO Formation. *J. Electrochem. Soc.* **1979**, *126*, 1914−1923.
(108) Baugh, L. M.; Baikie, A. R. Passivation of Zinc in Concentrated Alkaline Solution—II. Role Of Various Experimental Factors and the Distinction between the Solid-State and Dissolution—Precipitation Mechanisms. *Electrochim. Acta* **1985**, *30*, 1173−1183.
(109) Hugot-Le Goff, A.; Joiret, S.; Saidani, B.; Wiart, R. In-Situ Raman Spectroscopy Applied to the Study of the Deposition and Passivation of Zinc in Alkaline Electrolytes. *J. Electroanal. Chem. Interfacial Electrochem.* **1989**, *263*, 127−135.
(110) Cai, W. B.; Scherson, D. A. In Situ Raman Spectroscopy of Zinc Electrodes in Alkaline Solutions. *J. Electrochem. Soc.* **2003**, *150*, B217−B223.
(111) Holmberg, N.; Laasonen, K. Theoretical Insight into the Hydrogen Evolution Activity of Open-Ended Carbon Nanotubes. *J. Phys. Chem. Lett.* **2015**, *6*, 3956−3960.
(112) Lacnjevac, C. M.; Jaksic, M. M. Synergetic Electrocatalytic Effect of D-Metals on the Hydrogen Evolution Reaction in Industrially Important Electrochemical Processes. *J. Resear. Inst. Catalysis of Hokaidu University* **1983**, *31*, 7−33.
(113) Zhu, A. L.; Duch, D.; Roberts, G. A.; Li, S.; Wang, H.; Duch, K.; Bae, E.; Jung, K. S.; Wilkinson, D.; Kulinich, S. A. Increasing the Electrolyte Capacity of Alkaline Zn−Air Fuel Cells by Scavenging Zincate with $Ca(OH)_2$. *ChemElectroChem* **2015**, *2*, 134−142.
(114) Falk, U. S.; Salkind, A. J. *Alkaline Storage Batteries*; John Wiley & Sons Ltd.: London, 1969.
(115) Khasin, E.; Tzidon, D. *Zinc Electrode for Use in Rechargeable Batteries*. EU Patent 2834874, 2015.
(116) Jacus, R. J. *Aluminum Compound Additives To Reduce Zinc Corrosion in Anodes of Electrochemical Cells*. U.S. Patent 5034291, 1991.
(117) McBreen, J.; Gannon, E. The Electrochemistry of Metal Oxide Additives in Pasted Zinc Electrodes. *Electrochim. Acta* **1981**, *26*, 1439−1446.
(118) Gallaway, J. W.; Gaikwad, A. M.; Hertzberg, B.; Erdonmez, C. K.; Chen-Wiegart, Y. C. K.; Sviridov, L. A.; Evans-Lutterodt, K.; Wang, J.; Banerjee, S.; Steingart, D. A. An In Situ Synchrotron Study of Zinc Anode Planarization by a Bismuth Additive. *J. Electrochem. Soc.* **2014**, *161*, A275−A284.
(119) Parker, J. F.; Chervin, C. N.; Pala, I. R.; Machler, M.; Burz, M. F.; Long, J. W.; Rolison, D. R. Rechargeable nickel−3D zinc batteries: An energy-dense, safer alternative to lithium-ion. *Science* **2017**, *356*, 415−418.

DOI: 10.1021/acs.chemmater.7b00754
Chem. Mater. 2017, 29, 4819−4832